Desiccation cracking of heterogeneous clayey soil: experiments, modelling and simulations

Darith-Anthony Hun[a], Julien Yvonnet[a,*], Johann Guilleminot[b], Abdelali Dadda[c], Anh-Minh Tang[c], Michel Bornert[c]

[a] *MSME, Univ Gustave Eiffel, CNRS UMR 8208, F-77454 Marne-la-Vallée, France*
[b] *Department of Civil and Environmental Engineering, Duke University, Durham, North Carolina, USA*
[c] *Laboratoire Navier, Ecole des ponts, Univ Gustave Eiffel, CNRS UMR 8205, F-77455 Marne-la-Vallée, France*

Abstract

Experimental results for the cracking of heterogeneous clay samples during desiccation are reported, and an associated numerical model is developed for comparison. The clay samples contain embedded rigid inclusions to induce heterogeneous strain fields during drying. The crack paths and local strain fields are monitored during the desiccation process using digital image correlation. A numerical phase field model for crack initiation and propagation is introduced and compared with the experimental results. A qualitative agreement is found for the obtained crack paths, whereas discrepancies remain for the local strain fields. A discussion regarding the comparison between the experimental results and model is provided.

Keywords: Clay, shrinkage, desiccation, crack propagation,Digital Image Correlation, Finite Element Analysis, phase field method, Inclusions

1. Introduction

Desiccation crack patterns can be observed in several natural systems, including complex crack networks in dried blood, cracks in old paintings, T/Y-

⋆XXX.

*Corresponding author
Email address: julien.yvonnet@univ-eiffel.fr (Julien Yvonnet)

shaped cracks in dried mud, and polygonal terrain cracks [1]. In soil science, soil cracks typically serve as preferential paths for water movement or solute transport [2] and contribute to the progressive deterioration of earth structures [3].

To understand the mechanism governing the desiccation cracking of clayey soils, other than a few observations at the field scale, most previous experimental studies have focused on crack production in laboratory settings using processed clays, often from slurry states [4]. These studies have shown that desiccation cracking is a complex coupled suction-contraction process [5, 6, 7, 8, 9] that is sensitive to the boundary conditions (air relative humidity, ambient temperature, basal friction, clay layer thickness, etc.) and intrinsic soil properties (clay content).

Modeling the shrinkage crack process involves many challenges, including: (a) taking into account the multiphysics phenomena, (b) the possibly stochastic character of these phenomena, (c) the complex microstructure of the material, and (d) the inherent numerical difficulties related to the crack initiation, branching, and coalescence of many interacting cracks within the samples.

Many models and numerical techniques have been developed to reproduce the crack patterns during clay desiccation, including phenomenological spring models [10, 11, 12, 13, 14], discrete element method (DEM) models [15, 16, 17], cohesive zone models [18, 19, 20], mesh fragmentation techniques [21], and eXtended Finite Element Method (XFEM) models [22]. Recently, Hu et al. [23] developed a phase field model to simulate crack patterns during the shrinkage of thin films on substrates and proposed a stochastic model of a random field for the fracture toughness and fracture energy to model the random distributions of cracks. One advantage of the phase field method for simulating fractures [24, 25, 26] is that it relies on a continuum mechanics model and thus allows the introduction of different behaviors and coupling in a more versatile manner.

In all the aforementioned numerical studies, only homogeneous samples were considered. The sole exception was [23], in which the existence of a heterogeneous composition of the samples at a smaller scale was indirectly taken into

account through the stochastic description of the properties at the sample scale. Surprisingly, we are not aware of studies involving cracks in drying clay samples involving macro-scale heterogeneities. The objective of the present study is to conduct both experiments and modeling for this configuration. In the experiments, rigid inclusions are embedded into clay samples subjected to drying to analyze their influence on crack initiation and the final crack patterns. As in [27], where homogeneous samples were considered, digital image correlation is used to evaluate local strain fields during the entire process. A phase field crack propagation model is developed to simulate the process, and its predictions are compared with the experiments. A discussion of the agreement between the experiments and the model is provided.

The remainder of this paper is organized as follows. In Section 2, we describe the experimental setup for the desiccation of heterogeneous clay samples and provide the crack pattern and strain field results for different configurations. In Section 3, the numerical phase field fracture model is presented. In Section 4, the parameters of the model are identified based on the experimental results. Finally, a comparison between the experimental results and numerical predictions is provided in Section 5.

2. Experiments

2.1. Experimental setup

The novelty of the present experimental setup lies in the introduction of rigid inclusions within clay samples during the drying process to determine the influence of heterogeneities on the cracking process.

2.1.1. Material

The studied material is Romainville clay, which can be found in the East Paris Basin. Its ability to shrink, swell and crack causes significant damage to buildings, especially in periods of severe drought, and several study campaigns have been conducted [28, 29] to understand and analyze these phenomena. This

clay is composed of different sediments: illite, scmectite, carbonate, quartz, and feldspar . The physical properties of this clay are listed in Table 1.

Soil properties	Values
Density of solid phase [Mg.m^{-3}]	2.79
Liquid limit[a] [%]	77
Plastic limit[b] [%]	40
Plasticity index[c] [%]	37
USUC classification	CH
Clay ($< 2\mu$m) [%]	79
Clay composition	Illite and smectite
Specific surface area (methylene blue absorption) [m^2.g^{-1}]	340

Table 1: Physical properties of Romainville clay [30].

[a]Liquid Limit is the water content (mass proportion of water in the mixture) at which soil changes from a plastic to a liquid state

[b]Plastic Limit is the water content at the change from a plastic to a semisolid state.

[c]The plasticity index of a soil is the difference between its liquid and plastic limits.

2.1.2. Experimental method

For the experiments, the clay paste was conditioned as described in [30, 31]. The samples were prepared as follows.

Figure 1: Experimental samples: S_0, S_{1c}, S_1, S_3 and S_6. Underscript c indicates that the inclusion is centered.

- The clay was taken directly from the site (Romainville, Paris-Est, France) as a block.
- The material was cut into small 2 cm pieces and immersed in distilled water for a period of 24 h to liquefy it.

- Then, the whole set was passed through a 2 mm sieve to filter out the larger particles.

- The mixed sludge had a water content of approximately 170% at this stage, and it was poured into $D = 116$ mm diameter cups with a height $h_0 = 8$ mm. Several ($n = 1, 2, 3$ or 6) rigid inclusions (cylinders with circular cross sections made of polymethyl methacrylate (PMMA) and radius $r_{inc} = 8$ mm) were randomly placed, as illustrated in Fig. 1. The radius of the inclusions should be small enough (compared to that of the soil sample) to minimize the boundary effects on the interaction between the soil and the inclusions. At the same time, the inclusions should be sufficiently large to ensure good observation of the soil/inclusion interface using the technique employed in this study. Note that each cup into which the clay was poured was covered with a Teflon film on both the lateral walls and the bottom to limit the effects of friction on the surface, as shown in the right panel of Fig. 2 and the picture in Fig. 3.

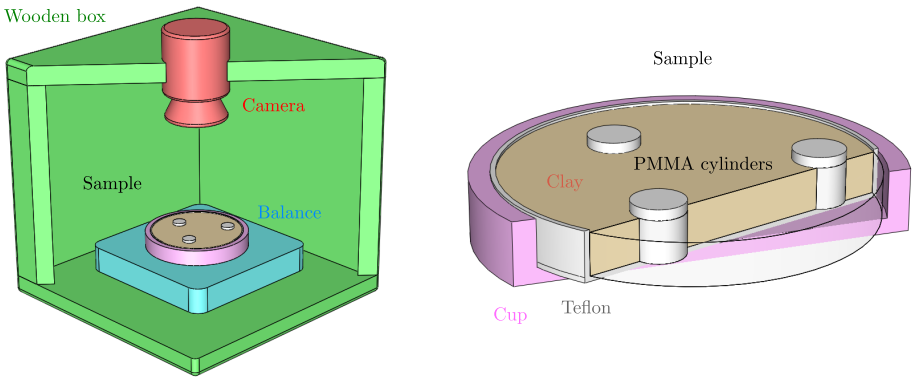

Figure 2: Experimental setup.

- The last step was the removal of air bubbles from the clay slurry. To this end, the samples were placed under vacuum for a period of 2 h and left covered for sedimentation for 72 h.

- Before starting the analysis, the supernatant water on the surface of the

clay mud sample was removed. The water content at $t = 0$ s of the test was $wc \sim 115\%$, and the clay sample thickness was $H = 8$ mm.

Then, the clay samples were placed in a wooden box with dimensions of $50 \times 50 \times 50$ cm to protect them from rapid thermal or moisture variations or from the surrounding ambient air. However, the box was not tight, and its internal hydrothermal conditions evolved with the current laboratory conditions. Several measuring tools were placed in the box, namely a scale, a thermometer, and an ambient moisture probe, which provided access to the water loss in the sample, temperature, and moisture throughout the drying test.

After 72 h, the sample was sufficiently stiffened. Black speckles were painted on its upper surface, providing an appropriate contrast to follow the shrinkage kinematics and measure the local deformation using the digital image correlation (DIC) technique. Images were recorded with a digital camera (Canon EOS TTL camera, equipped with an 18–55 mm zoom lens, providing 8-bit color images with 5184×3456 pixels). Image acquisition was performed at time intervals of $\Delta t = 10$ min. Various samples (with different inclusion numbers and configurations) were considered, as shown in Fig. 2 (left panel) and Fig. 3.

- S_0: a clay sample without inclusion.
- S_{1c}: a clay sample with a single centered inclusion.
- S_1, S_3, S_6: clay samples containing $n = 1, 3, 6$ randomly-distributed inclusions.

On an orthonormal frame $(0; \mathbf{x}, \mathbf{y})$ whose origin is at the center of the sample, the inclusions are located at the coordinates (-1.90,-24.7) mm for S_1; (19.87,3.18), (-20.84,19.35), and (-24.30,20.17) mm for S_3; and (-22.9,-30.7), (24.26,-8.63), (-2.46,-2.72), (-29.82,19.01), (2.20,27.36), and (32.6,31.40) for S_6.

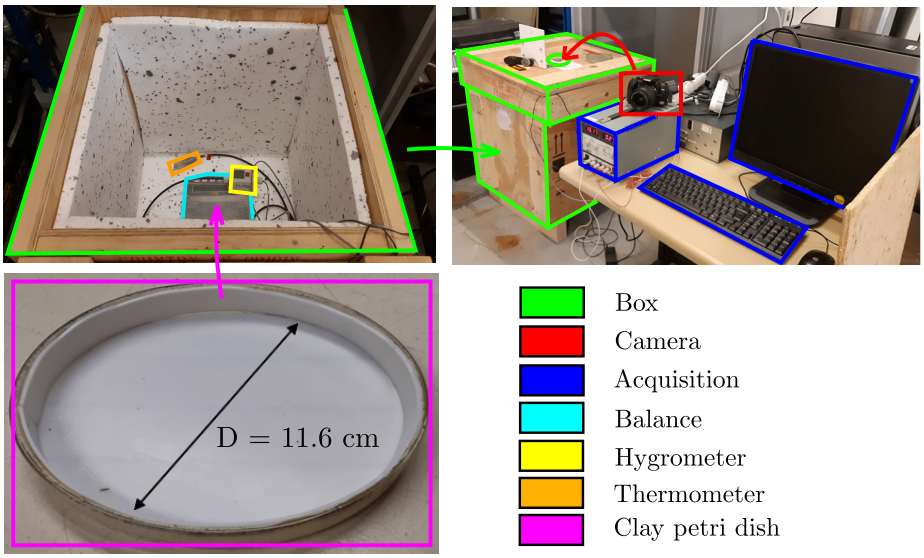

Figure 3: Experimental setup photos.

2.1.3. DIC image analysis

The obtained images were analyzed using DIC [32] to evaluate the 2D displacement and deformation field on the upper surface of the sample. An in-house image correlation software (CMV) was used to process the images converted into gray levels. The software is based on a local DIC formulation using the zero-centered normalized cross-correlation criterion, an affine shape function of the displacement field within correlation windows, and biquintinc interpolation of the gray level to achieve subpixel accuracy for evaluation of the displacement fields. In-plane transformation gradient components were obtained from discrete evaluations of the displacement at the centers of adjacent non-overlapping correlation windows using relations detailed by Allais et al. [33]. Two quantities of interest are analyzed in the following: the spherical (or hydrostatic) strain, ϵ_S, and the deviatoric strain, ϵ_D:

$$\epsilon_S = \frac{1}{2}\mathrm{tr}(\boldsymbol{\epsilon}) \ , \ \epsilon_D = \frac{2}{3}(\bar{\epsilon}_2 - \bar{\epsilon}_1) \ , \tag{1}$$

where $\bar{\epsilon}_1$ and $\bar{\epsilon}_2$ ($\bar{\epsilon}_2 \geq \bar{\epsilon}_1$) are the eigenvalues of the 2D Green-Lagrange strain tensor, and $\mathrm{tr}(\epsilon) = \epsilon_1 + \epsilon_2$ measures the variation of the surface. It is empha-

sized that ϵ_s is different from the volume variation, which cannot be measured based on purely surface investigations. These quantities were evaluated for a gauge length limited by the typical length scale of the speckle painting. With approximately 2700 pixels along the diameter of the cup and speckle sizes that allowed the use of 30-pixel-wide correlation windows, there were approximately 100 independent local evaluations of the 2D displacement field along such a distance. The accuracy of the measurements was limited by the image quality, noise, and other artifacts that are not detailed here; however, the accuracy was significantly better than 1%, and is thus sufficient to quantify the heterogeneity of the investigated strain fields.

2.2. Results

2.2.1. Evolution of experimental conditions

The first results, shown in Fig. 4, indicate the conditions of the experiment, with an ambient relative moisture of $RH = 48\% \pm 6$, a temperature of $T = 20 \pm 2^o$C, and water content (ratio of the weights of water and clay) of $wc = 115 - 10\%$. The relatively small variations in these parameters from one sample to another show that the experiments were carried out under stable, repeatable conditions. Even if the conditions differed slightly between samples, it turns out that the drying rate was slow (the tests lasted approximately one week) with respect to the typical time of the moisture transfer within the clay matrix. At this stage, we consider that the water content in the clay material can be considered uniform and is directly given by the overall mass loss quantified by the scale. The latter was almost linear with time, as shown in Fig. 4 (c).

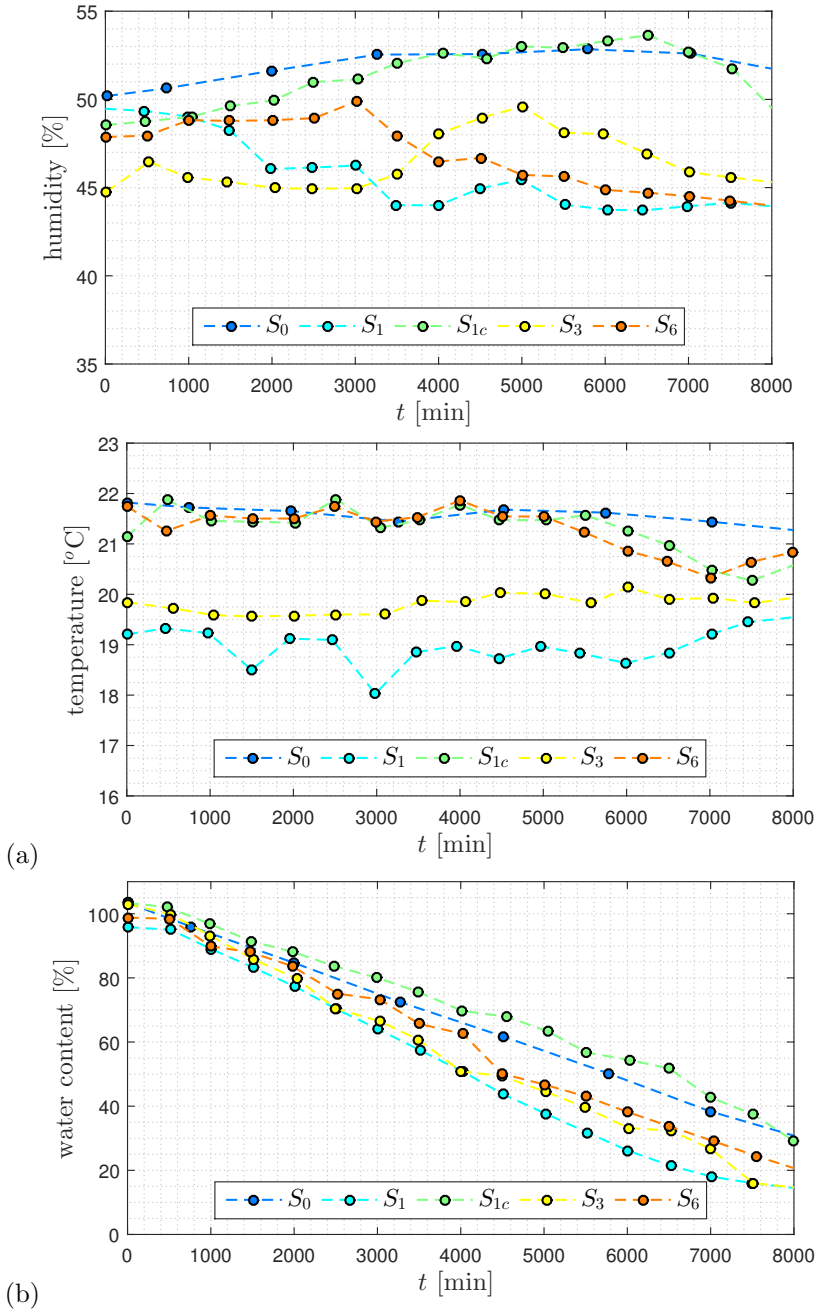

(a)

(b)

(c)

Figure 4: (a) Moisture, (b) temperature and (c) water content during drying of the sample.

2.2.2. Crack process

In the experiments, three characteristic times $t_1 = 4000$ min, $t_2 = 6000$ min, and $t_3 = 8000$ min were chosen for the observations of all samples. These times correspond, respectively, to a time when cracks have not yet initiated, a time when cracks start to initiate, and a time when cracks have propagated through the sample. The drying process lasted 72 h.

Figs. 5,6,7,8, and 9 show the crack patterns in the samples at times t_1, t_2, and t_3. The crack paths obtained for each specimen show some similar propagation pattern features. The cracks initiate near the rigid inclusions and propagate toward the outer edge of the specimen. Once all of the cracks have propagated, the material shrinks over its entire range, and the material is broken down into small independent pieces. It should be noted that the crack paths over the entire test set consist of three or four branches with angles between these branches, θ_c, such that $\pi/2 \leqslant \theta_c \leqslant \pi/3$.

2.2.3. Strain analysis

In this section, the deformation maps obtained using the DIC technique are presented for the three characteristic times t_1, t_2, and t_3. These maps were defined for the set of samples $(S_0, S_{1c}, S_1, S_3, S_6)$ and show the spherical and deviatoric strains in the samples. The spherical and deviatoric deformations are defined as Eq. (1). The intensities of these strains are indicated by colors that are associated with the kinematics of the drying cracking process in qualitative and quantitative ways.

For later purpose, we define three characteristic regions within the sample as illustrated in Fig. 10.

- R_B is a ring surface next to the external and inclusion surfaces,
- R_+ is another ring surface interior to the external portion of R_B,
- R_i is the rest of the interior surface.

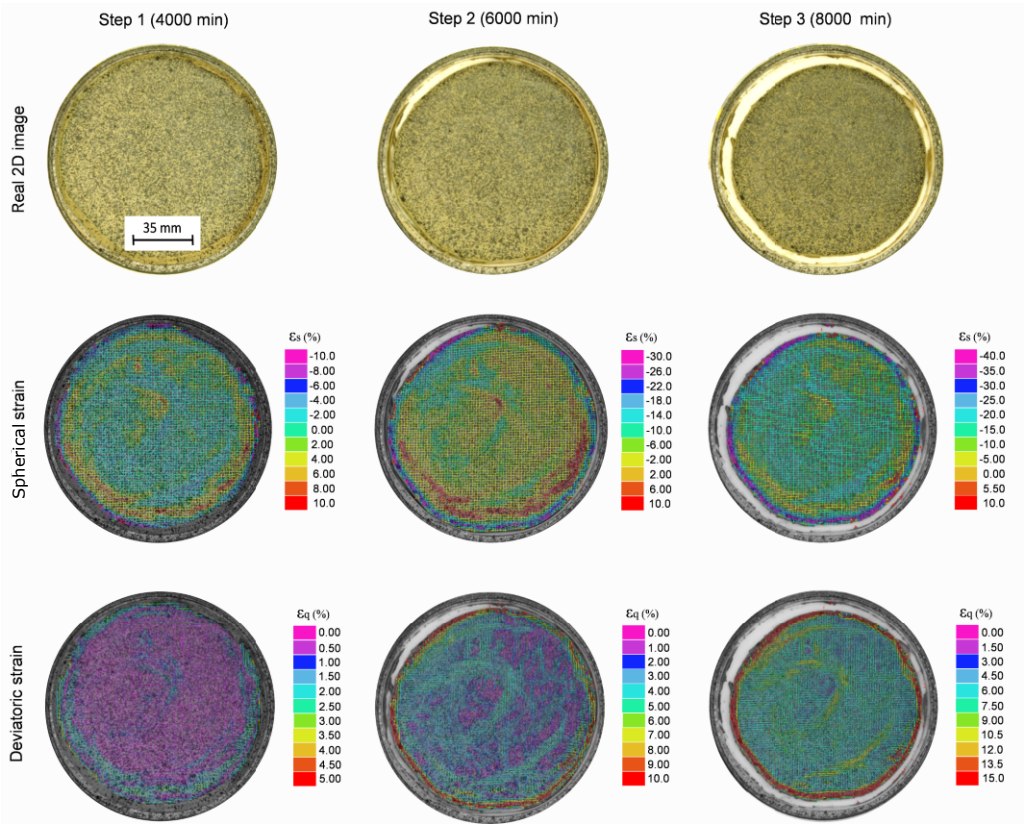

Figure 5: S_0 test with shrinkage, spherical and deviatoric strains for t = 4000, 6000, and 8000 min.

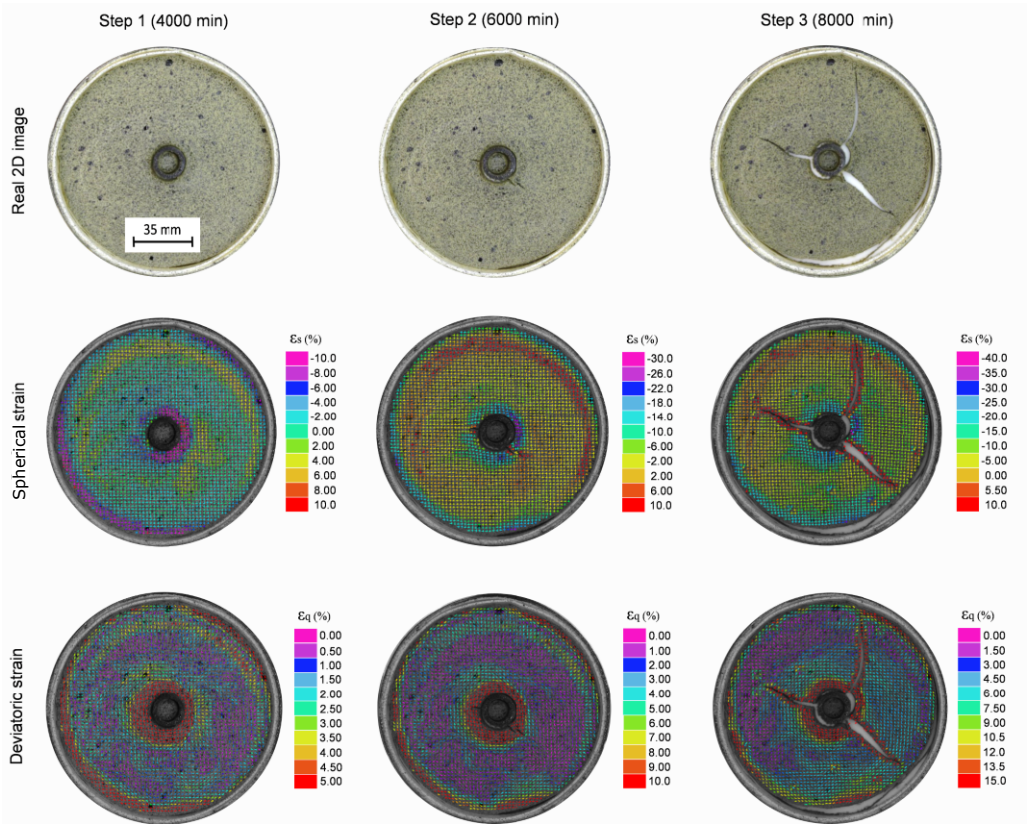

Figure 6: S_{1c} test with shrinkage, spherical and deviatoric strains for t = 4000, 6000, and 8000 min.

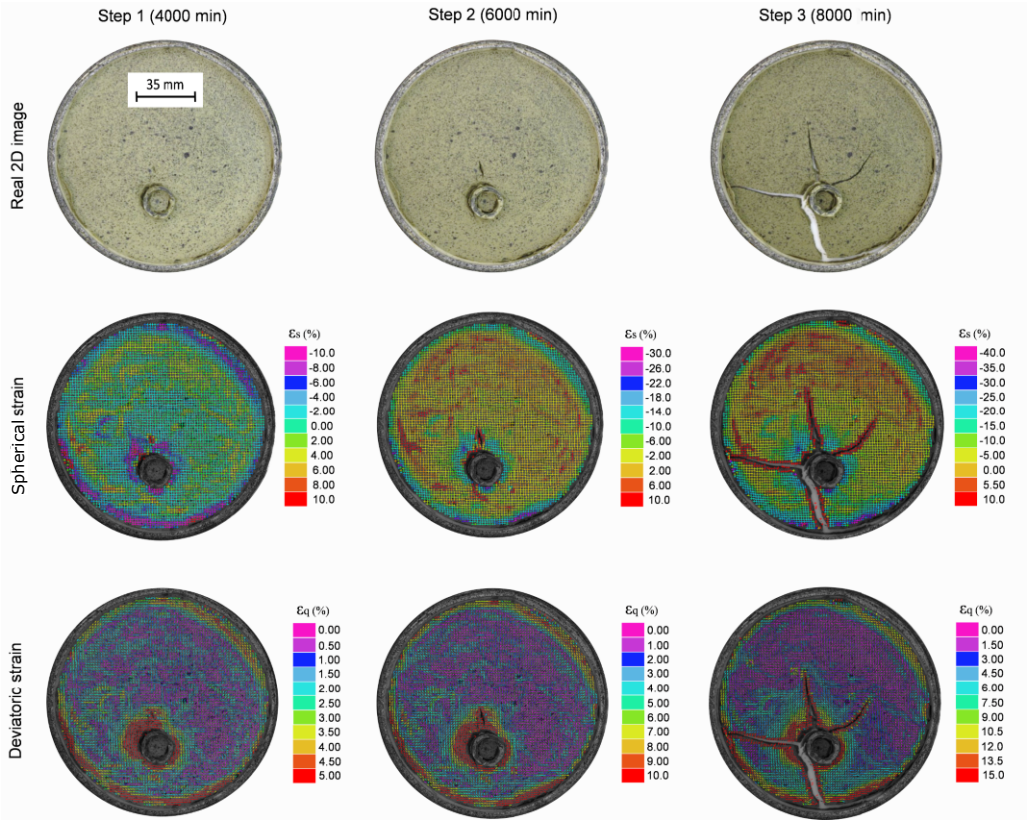

Figure 7: S_1 test with shrinkage, spherical and deviatoric strains for t = 4000, 6000, and 8000 min.

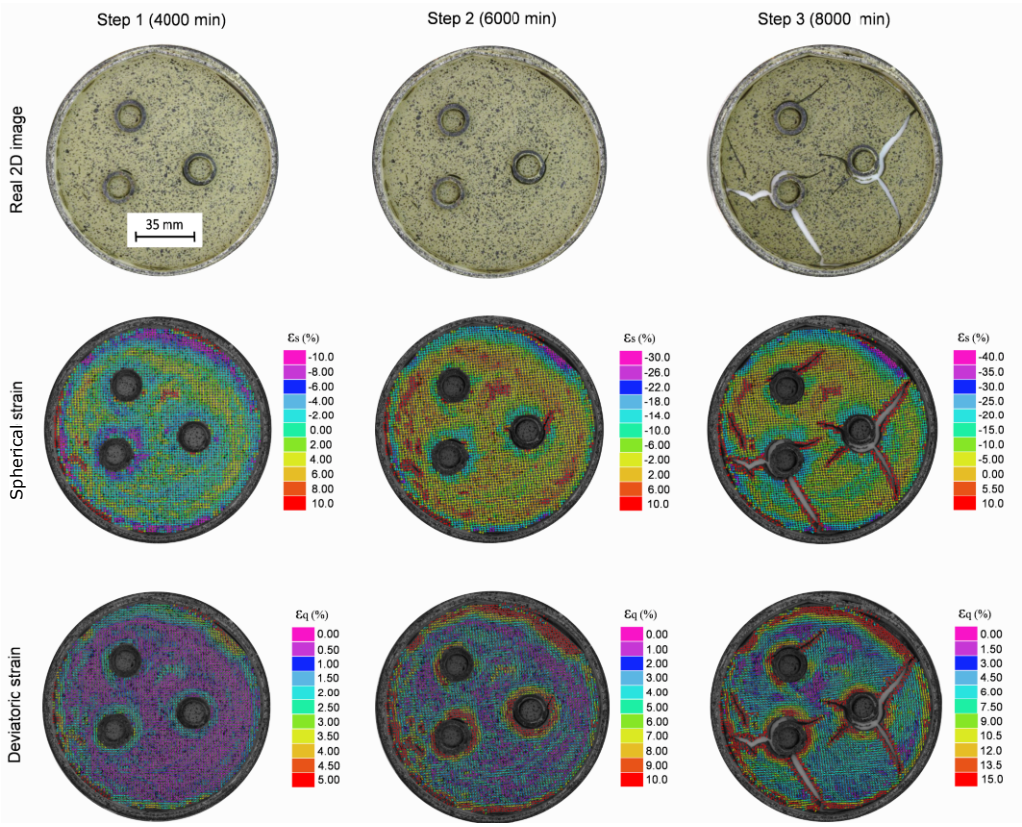

Figure 8: S_3 test with shrinkage, spherical and deviatoric strains for t = 4000, 6000, and 8000 min.

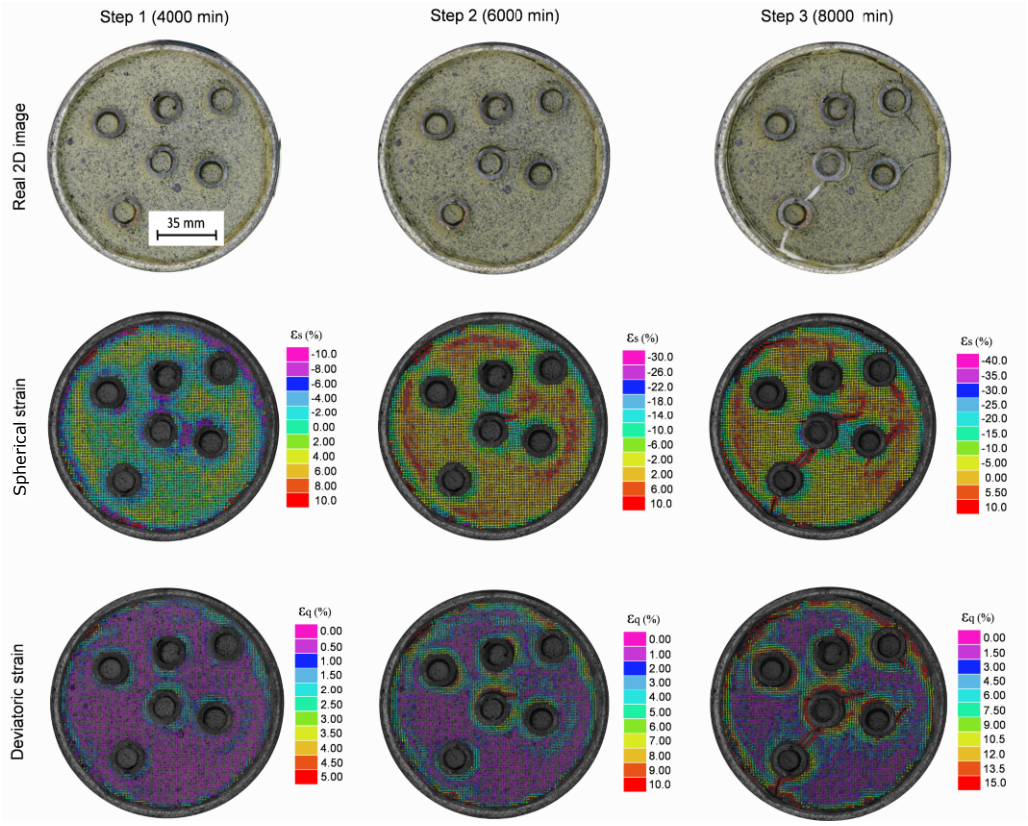

Figure 9: S_6 test with shrinkage, spherical and deviatoric strains for t = 4000, 6000, and 8000 min.

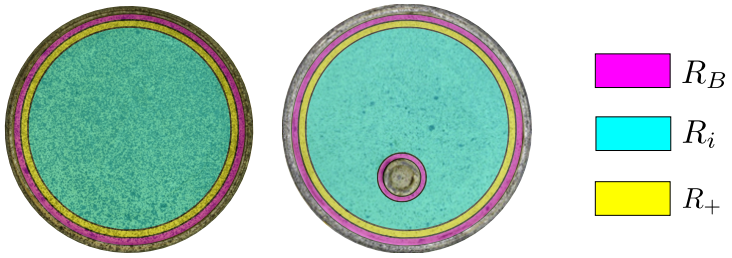

Figure 10: Definition of specific zones of interest in the clay samples.

S_0 test

In the first test, the sample does not contain rigid inclusions (see Fig. 1). From Fig. 5, we can observe that the spherical and deviatoric deformation fields remain roughly constant in the interior of the sample.

- First, at t_1, the spherical deformation is negative (as expected) in R_i, with $\epsilon_S \sim -2\%$, and is roughly homogeneous except in $R_B \cup R_+$. A positive deformation is observed in R_+, while another negative strain zone appears in R_B with a value different from that in the rest of the sample. The deviatoric strain is almost zero in the central area of R_i, indicating a purely radial surface deformation, as expected in a homogeneous shrinkage process. However, the deviatoric strain is non-zero with $\epsilon_D \sim 2\%$ in $R_B \cup R^+$. These heterogeneities may be explained by the adhesion of the sample material to the external boundary of the dish.

- Second, at t_2, debonding occurs at the top left external boundary of the sample. The spherical and deviatoric strain maps are then perturbed. In R_i, the spherical strain remains negative, with $\epsilon_S \sim -2\%$, while the strain is no longer homogeneous and compression occurs ($\epsilon_S \sim -14\%$) in R_+. Regarding the deviatoric strain, the main observations made at t_1 remain valid, whereas more localized regions and heterogeneities appear in the central region.

- In the last step, t_3, the sample is fully detached form the dish boundaries. The strain field remains globally radial, and more pronounced heterogeneities appear.

S_{1c} test

The results for the S_{1c} test involving a centered inclusion are presented in Fig. 6.

- At step $t = t_1$, we observe an additional characteristic zone near the inclusion boundary (R_B). In this zone, important compressive strains occur, with $\epsilon_S = -10\%$, which is equal to the deformation on the outer edge. As in the homogeneous case (S_0 test), a zone R_i of weakly negative strain $\epsilon_S \sim -2\%$ is observed. Then, in (R_+), we observe an extension with ($\epsilon_D \sim 4\%$). The deviatoric strain is almost zero except near the boundaries in R_B, with $\epsilon_D \sim 5\%$. We can see that the perturbations induced by the inclusion are localized in a radial area with a diameter of roughly three times the diameter of the inclusion.

- At $t = t_2$ debonding occurs at the bottom of the sample. The strain maps are modified in the same manner as in the case without an inclusion. In the subregion R_B around the inclusion, the shrinkage is high ($\epsilon_S \sim -14\%$). In R_i, a small shrinkage remains ($\epsilon_S \sim -2\%$). Then, in R_+, the situation is similar to that without inclusions. The deviatoric strain increases up to $\epsilon_D \sim 10\%$ in R_B and remains quite low ($\epsilon_D < 4\%$) in $R_+ \cup R_i$. The debonding at the lower part also induces a local increase in the deviatoric strain.

- Finally, at $t = t_3$, the clay separates from the external boundary along 40% of the external surface. In contrast to the previous case (S_0 test), the upper half of the ring R_+ remains in extension ($\epsilon_S \sim 5\%$). In the other part, as in the previous observation, there is a strong zone of shrinkage ($\epsilon_S \sim -20\%$) on the border R_B and a less intense zone ($\epsilon_S \sim -5\%$) in the remaining area R_i. For the deviatoric strain, high strains are again observed in R_B (outer part and near the inclusion). The deviatoric strain is almost null in areas far from the borders and the inclusion, especially in the non-debonded half of the sample.

It should also be noted that the very high values of the deviatoric strains at the borders of the cracks are post-processing artifacts and should not be interpreted as local deformation of the clay. Indeed, the displacement jump over the crack is integrated in the local evaluation of the strain, which is based on some finite differences (see [33] for the details about the calculation of the strain).

S_1 test

The main difference between this test and the previous test is the lack of symmetry induced by the position of the inclusion.

- At $t = t_1$, as in the previous cases, the localized strain areas are located on the edges R_B of the sample and exhibit strong compression ($\epsilon_S \sim -10\%$). It can also be observed that the field surrounding the inclusion is also more heterogeneous than in the S_{1c} sample. In this test, the ring R_+ does not appear clearly, and the remaining surface R_i is a mixture of low-intensity positive and negative surface stresses $|\epsilon_S| < 5\%$. For the deviatoric strain, the intensity is relatively low, as in the previous samples, high $\epsilon_D \sim 5\%$ at the outer areas R_B, and then low again in the inner area $R_+ \cup R_i$, but with some noticeable heterogeneities.

- At $t = t_2$, ϵ_S reaches -14% in R_B near the external boundary. The R_+ zone does not appear to develop in this case. In R_i, $\epsilon_S \sim 2\%$; nevertheless, some scattered zones have more localized values, where $\epsilon_S \sim 10\%$. Regarding the deviatoric strain, the intensity continues to increase on the edges R_B and remains small on the interior surface $R_+ \cup R_i$.

- At the last step $t = t_3$, the specimen again exhibits strong shrinkage $\epsilon_S \sim 20\%$ on the outer edges R_B. The inner zone R_i has extensional strains $\epsilon_S \sim [5\%, 10\%]$, which are larger than those in the previous S_0 and S_{1c} tests but remain relatively low. For the deviatoric strain, the trend seems to be similar to those in the previous cases.

In this sample with an off-center inclusion, debonding at the outer edge is limited. Adhesion induces very strong compression strains in areas very close to the boundaries, together with extensive strains of lower intensity in larger zones and far from the edges. Some fluctuations are observed in these areas in extension, but are not associated with strong deviatoric strains. The inclusion located in the lower part first generates localized deviatoric strains and then cracks. This allows the surrounding clay to shrink, first in the neighborhood near the inclusion and then in the larger areas around the cracks.

S_3 and S_6 tests

The final tests were carried out to investigate the effects of interactions between several inclusions during the drying process (see Fig. 8 and Fig. 9).

- At $t = t_1$, for both samples, a strain localization is observed on the surface near the inclusions and near the external boundary R_B with $\epsilon_S \sim -10\%$ and $\epsilon_D \sim 2\%$. These values gradually decrease and finally vanish far from the sample and inclusion edges. However, the symmetry of the revolution of this expansive strain field around the inclusions is broken in sample S_6, while it is essentially preserved in S_3, where the distance between the inclusions is larger. Within the R_+ zone, $\epsilon_S \sim 4\%$.

- In the subsequent state at $t = t_2$, the heterogeneities in the stain field are increased. It can be observed that there is no significant additional debonding at the outer edge of the sample, unlike in samples S_0 and S_{1c}.

- At the final stage $t = t_3$, the extension zones $R+$ have been replaced by contraction zones or cracking. A few expansive zones remain, which are the locations of the secondary cracks.

A general observation is that the overall features of the strain field around the inclusions in S_3 are similar to those observed in S_1 and S_1c. This is also true for the crack geometries: cracks initiated from inclusions do not interact with the others. However, this is not true for the S_6 sample, in which positive ϵ_S

strains are not observed between the closer inclusions. In addition, the cracks have different features: some are generated in areas with positive ϵ_S, and some clearly connect two inclusions.

3. Numerical model

3.1. Phase field mode of crack shrinkage

In this study, crack initiation and propagation are modeled using the phase field method [24, 25, 26, 34, 35, 36]. In this context, crack discontinuities are represented by a regularized approximation through a field $d(\mathbf{x})$ associated with damage. A value of $d = 0$ corresponds to undamaged material, whereas $d = 1$ is associated with fully damaged material. The main advantage of this method is that the initiation, propagation, and merging of complex crack patterns can be achieved without any special numerical treatment using classical finite elements. In addition, this formulation naturally regularizes the strain localization and does not suffer from mesh-dependency issues. The main concept of this approach is to formulate the damage problem in a variational manner. Starting from the energy, minimization with respect to the displacement field on one side and maximization of the dissipation on the other side under the constraint of irreversible damage evolution yields two sets of coupled equations whose solution provides the displacement field and the damage field $d(\mathbf{x})$ at each load increment. Here, we formulate this problem in the context of finite strains as shrinkage can induce large deformations. In addition, the constitutive law is modified to consider compressive hydric strains related to shrinkage.

Considering a domain $\Omega \subset \mathbb{R}^d$, $d = 2, 3$ containing the sample material in its initial configuration and its boundary $\partial\Omega$ with an external normal unitary

vector $\mathbf{N}$, the equations are summarized as follows:

$$\begin{cases} \nabla_X \cdot \boldsymbol{P} = 0 \text{ on } \Omega \\ \boldsymbol{S}(\boldsymbol{E}(\boldsymbol{u}), \boldsymbol{E}_h, d) = \frac{\mathcal{D}(d)}{h^2}\mathbb{C}(\boldsymbol{E} - \boldsymbol{E}_h) \\ \boldsymbol{E}_h = \alpha \boldsymbol{I} \\ \boldsymbol{u} = \bar{\boldsymbol{u}} \text{ on } \partial\Omega_u \\ \boldsymbol{P} \cdot \boldsymbol{N} = \bar{\boldsymbol{t}} \text{ on } \partial\Omega_t, \end{cases} \tag{2}$$

and

$$\begin{cases} 2(1-d)\mathcal{H} - \frac{g_c}{\ell}\{d - \Delta_X d\} = 0 \text{ on } \Omega \\ \nabla_X d(\boldsymbol{x}) \cdot \mathbf{N} = 0 \text{ on } \partial\Omega. \end{cases} \tag{3}$$

Above, $\mathbf{P}$ and $\mathbf{S}$ are the first and second Piola-Kirchhoff stress tensors, respectively, which are related by $\mathbf{P} = \mathbf{FS}$, where $\mathbf{F} = \mathbf{I} + \nabla_X \mathbf{u}$ is the gradient of the transformation tensor, $\nabla_X(.)$ is the gradient with respect to the initial configuration, and $\nabla_X \cdot (.)$ is the divergence operator with respect to the initial configuration. The boundaries $\partial\Omega_u$ and $\partial\Omega_t$ denote the portions of $\partial\Omega$ where the displacements $\bar{\mathbf{u}}$ and tractions $\bar{\mathbf{t}}$ are prescribed, respectively. In Eq. (2), $\mathcal{D}(d)$ is a degradation function used to penalize the elastic tensor $\mathbb{C}$, and it is defined here as $\mathcal{D}(d) = (1-d)^2$. Furthermore, $\mathbf{E}$ is the Green-Lagrange strain tensor, and $\mathbf{E}_h$ is the hydric strain, with $\mathbf{I}$ as the identity second-order tensor, and α as an evolution parameter defined later in Section 4.3. Next, in Eq. (3), g_c is the fracture toughness, ℓ is a regularization length parameter controlling the width of the crack, and $\Delta_X(.)$ is the Laplacian operator in the reference configuration. The function $\mathcal{H}$ is a history function, which is introduced to satisfy the irreversibility of damage. It is expressed as (see [37]):

$$\mathcal{H}(\mathbf{x}, t) = \max_{\tau \in [0,t]} \{\Psi(\boldsymbol{E}(\boldsymbol{x}, \tau))\} , \tag{4}$$

with

$$\Psi(\boldsymbol{E}) = \frac{\lambda}{2}\left(\langle Tr(\boldsymbol{E})\rangle\right)^2 + \mu Tr\{(\boldsymbol{E})\} , \tag{5}$$

where λ and μ are the elastic Lamé's parameters of the clay material in its solidified, uncracked state. The corresponding weak forms, which are applied

to solve the problem using finite elements, are provided as follows:

$$\int_{\Omega} \boldsymbol{S}(\boldsymbol{E}(\boldsymbol{u}), \boldsymbol{E}_h, d) : \delta\boldsymbol{E}(\boldsymbol{u}, \delta\boldsymbol{u})\, d\Omega = \int_{\partial\Omega_N} \overline{\boldsymbol{t}} \cdot \delta\boldsymbol{u}\, d\Gamma \ , \tag{6}$$

and

$$\int_{\Omega} \left[\left(\frac{g_c}{\ell} + 2\mathcal{H} \right) d\ \delta d + g_c \ell \nabla d \cdot \nabla(\delta d) \right] d\Omega = \int_{\Omega} 2\mathcal{H}\delta d\ d\Omega \ . \tag{7}$$

These equations are solved alternately in a so-called "staggered" scheme (see [26]). More details regarding the phase field method and its numerical solution procedures using FEM can be found in, e.g., [26, 36].

3.2. Numerical Finite Element model

The numerical model is schematically described in Fig. 11. For a given test (i.e., for one sample and a given number and distribution of inclusions), a digital twin is defined using the experimental data described in Section 2. Based on the measurements, the initial radius of the cylindrical cup is set to $r_0 = 58$ mm, the radius of the inclusions is $r_{inc} = 8$ mm, and the height is $h_0 = 8$ mm. The clay material is contained within the domain Ω (see Fig. 11 (a) for an example with three inclusions).

To account for the damage mechanisms observed experimentally, the boundary conditions are defined as follows.

- Zero-displacement Dirichlet boundary conditions are initially applied on $\partial\Omega$, while stress-free conditions are considered at the boundaries of the inclusions, denoted collectively as $\partial\Omega'$. Shrinkage is then induced by increasing the eigenstrain $\boldsymbol{E}_h = \alpha_h \boldsymbol{I}$ (see Eq. $(2)_3$), where the parameter α_h is defined in Section 4.3. The problem (2) is then solved at each time step.

- When the condition $d = 1$ is met for a subset $\partial\Omega_{deb}$ of $\partial\Omega$ (note that $\partial\Omega_{deb}$ is not connected in general), the boundary conditions on $\partial\Omega_{deb}$ are switched to free traction with the aim of modeling the sudden debonding observed during the experiments.

- Concerning the bottom of the sample, denoted by $\partial\Omega_{z=0}$, the boundary conditions are vertically fixed to 0, but are free within the $\mathbf{e}_x$-$\mathbf{e}_y$ plane.

From a computational standpoint, both 2D plane strain and 3D simulations are carried out. The geometry of the sample is discretized using

- T3 elements in the 2D case, resulting in a mesh with $N^d_{dof} = 15 \times 10^3$ degrees of freedom for the damage problem and $N^e_{dof} = 2N^d_{dof}$ degrees of freedom for the elastic problem; and

- T4 elements for the 3D case. The mesh contains $N_e = 400 \times 10^3$ elements, corresponding to $N^d_{dof} = 80 \times 10^3$ degrees of freedom for the damage

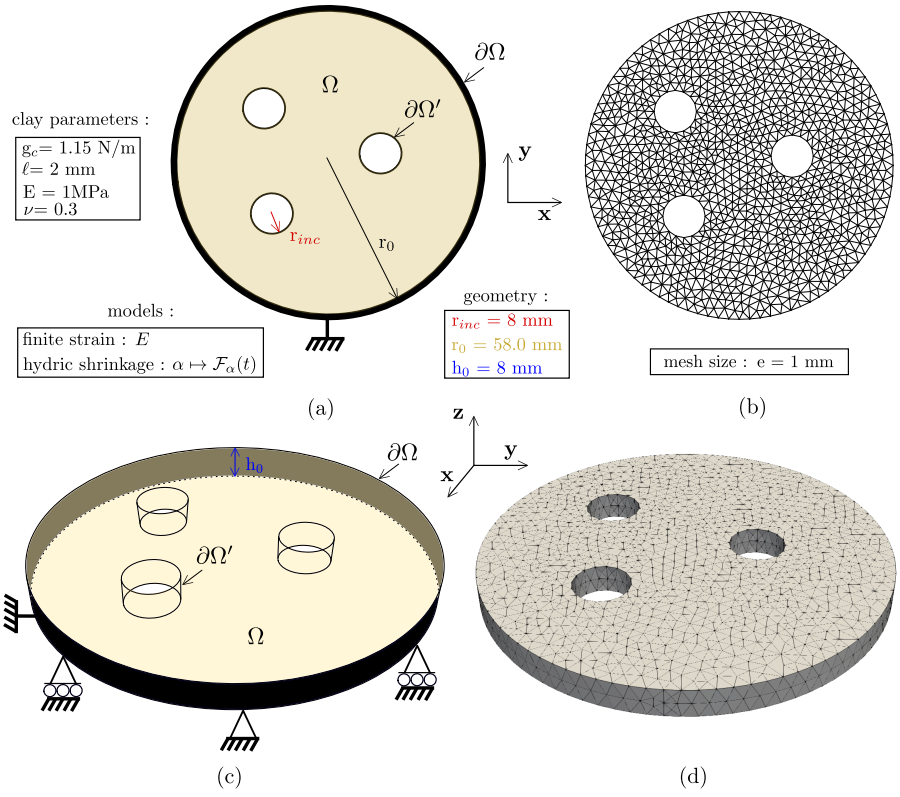

Figure 11: Numerical FEM model for a specific configuration: (a) geometry and boundary conditions for the 2D model; (b) 2D mesh; (c) geometry and boundary conditions for the 3D model; (d) 3D mesh.

problem and $N^e_{dof} = 3 \times N^d_{dof}$ for the elastic problem.

An in-house implementation combining C++ and MATLAB codes was used. The computational times on a computer equipped with an Intel(R) Xeon (R) platinum 8168 CPU (with 1 TB of RAM and 2×24 cores rated at 2.7 GHz) ranged from 0.7 to 3 s per time step for the 2D case and from 55 to 150 s for the 3D case. The total computational times based on 1000 time steps were 2.5 h and 42 h for each 2D or 3D case, respectively.

4. Model identification

In this section, we provide the values of the model parameters and identification procedures when required.

4.1. Mechanical parameters

The mechanical parameters used in the model described in Section 3 were extracted from the literature. The Young's modulus for the clay material was taken as $E = 1$ MPa according to the study in [20], in which a simulation of crack propagation in the 2D plane was conducted with a cohesive zone model on clayey materials. This modulus was defined experimentally in [38], where a variable Young's modulus was defined as a function of the compaction of the material. In our clayey material, we assumed a similar situation when the material solidified according to the decrease in the water content. In [20], the modulus was averaged over the compaction range. This hypothesis was retained for the numerical study. Other authors [39] have proposed a variation of this modulus according to the water content in the experimental investigations of [40] on Barcelona soil and [41] on Bioley clayey silt. The Poisson's ratio was chosen as $\nu = 0.3$ [20].

4.2. Fracture parameters

The damage parameters used in the following simulations require estimation of the toughness g_c and the regularization length ℓ, as this parameter is interpreted here as a material parameter (see the discussion in [42]). Many authors

have studied the impact of water content on crack resistance. In [43], a comprehensive review of the environmental factors in the cracking process was provided through multiple experiments. More specifically, numerous studies have allowed the identification of the parameters for linear mechanical fracture models through experiments (see [44, 45, 41]). The parameters used are often the stress intensity factor K_I or the tensile limit stress σ_t, which can then be theoretically related to the pair of parameters (g_c, ℓ) in the phase field method (see [42]). Following these studies, a numerical investigation of clay desiccation using the phase field method was reported in [39]. The parameters used were the toughness depending on the water content ($g_c = 1.12$ $(wr = 0\%) - 1.71$ $(wr = 100\%)$ N/m) and a constant regularization length $\ell = 2$ mm. In our study, we consider the toughness as a constant, with $g_c = 1.15$ N/m, and the regularization length is set as $\ell = 2$ mm.

4.3. Hydric model

In this section, we describe the procedure for identifying the function $\alpha_h(t)$ of the coupled hydric shrinkage model (see Eq. (2)) based on the experiments. Experimental test S_0 described in Section 2.2.3 was used, where a homogeneous circular sample was considered. In this test, the sample shrank without cracking and remained circular during the drying process. Denoting the experimental radius as $R^{\exp}(t)$, it is possible to record the evolution of this radius as a function of time. This evolution is illustrated in Fig. 5 and the radius is reported in Fig. 12 (left).

The experimental evolution of the radius (red dots) was fitted using the R_t function, defined as follows:

$$R_t(t) = A(1 + \tanh(B(t - \phi)) + R_\infty, \tag{8}$$

Here, A is the amplitude, which is defined as

$$A = \frac{1}{2}(R_\infty - R_0), \tag{9}$$

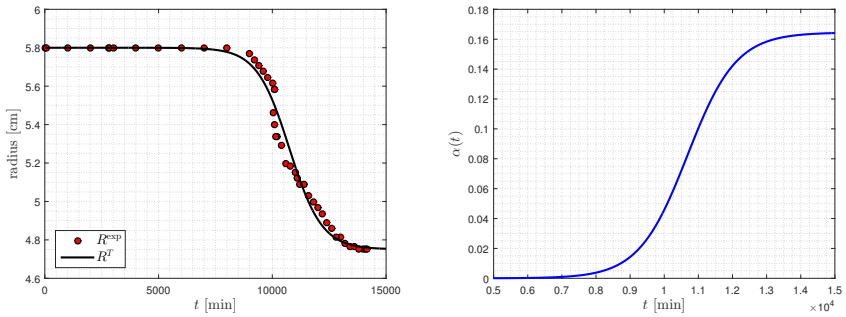

Figure 12: (Left) Identified R_t function, (right) the identified shrinkage parameter α_h.

where R_0 and R_∞ denote the initial and final radii, respectively. B is the transition time between radii R_0 and R_∞ according to

$$B = \frac{1}{\Delta T} \ , \tag{10}$$

where ΔT is the transition time, and ϕ represents the shift in the hyperbolic tangent function. The other parameters are obtained for $\phi = 10750$ and $B = 7.0.10^{-4}$, corresponding to $\Delta T = 1.4.10^3$. Fig. 12 shows both the experimental results and the fitted radius function (black line).

Then, the parameter α_h was identified using the numerical model presented in the previous section without any inclusions (sample S_0, see Fig. 1); it is directly related to the radius shrinkage measurements. Thus, we obtained the time function for α_h, as illustrated in Fig. 12 (right). In the following simulations, the identified function $\alpha_h(t)$ is used, even for the simulations involving cracks, bearing in mind that this is a strong simplification of the model. The other parameters are summarized in Table 2.

E	ν	g_c	ℓ	e
1 MPa	0.3	1.15 N/m	2 mm	1 mm

Table 2: Identified parameters for the shrinkage model.

5. Comparison between experiments and simulations

In this section, the numerical model presented in Section 3 is compared with the experimental results presented in Section 2. In all cases, comparisons are made at time t_3 (see Section 2.2.2).

5.1. Final morphology of crack patterns

Comparisons between the final crack patterns in the experiments and those obtained with the simulation model are presented in Figs. 13-16. A summary of the observations and qualitative agreement is provided in Table 3. Based on these results, we can note that a qualitative agreement regarding the final crack patterns is obtained. In the different cases, the simulation model correctly captures most of the phenomena, including the initiation of cracks from the inclusion boundaries and radial development of cracks. Moreover, when many inclusions are involved, the cracks merge between the inclusions and then propagate through the external boundary of the sample. In the 3D simulations, there is disagreement in the crack morphology in the case of a single inclusion: while three cracks were observed in the experiment, two branching cracks propagate in the model results. One possible reason is the implementation of a zero-displacement boundary condition along the external boundary in the 3D model while the interior of the sample is allowed to shrink along the z vertical direction, which creates a more complex strain state. In spite of this, most of the qualitative results are found to be in fairly good agreement with the experimental observations. However, it is worth noting that the experimental and simulation times at which the images are shown are not always the same. This is mainly because the shrinkage model (12) was identified experimentally on a sample without any inclusions. Thus, the present shrinkage model does not properly consider the interactions with other inclusions. Therefore, the simulations that exhibited the best agreement with the experiments were taken for times that did not always match those of the experiments. We are aware that the present shrinkage model is overly empirical and that it should be improved

by using more micro-mechanical foundations to consider the hydro-mechanical coupling and allow its use in more complex configurations.

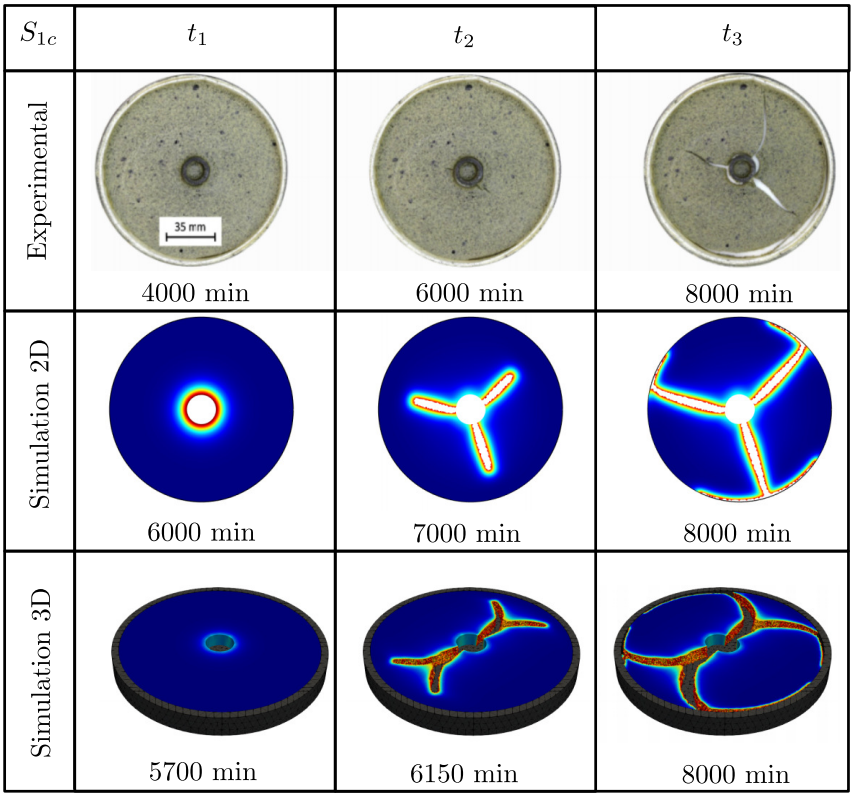

Figure 13: Crack pattern in S_{1c}.

5.2. Spherical strains

In Figs. 17-20, the local spherical strains measured experimentally as described in Section 2.2 are compared with the numerical simulations.

A global negative shrinkage was obtained in the experiments and is well reproduced in the simulations (see Fig. 17). This agreement is less obvious in the case of multiple inclusions (see Figs. 19 and 20) where the local fields are strongly perturbed by the open cracks. Furthermore, we note that even in the S_{1c} case, regions of compressive strain localization are observed in the experiments near the external boundary, but these are not reproduced in the

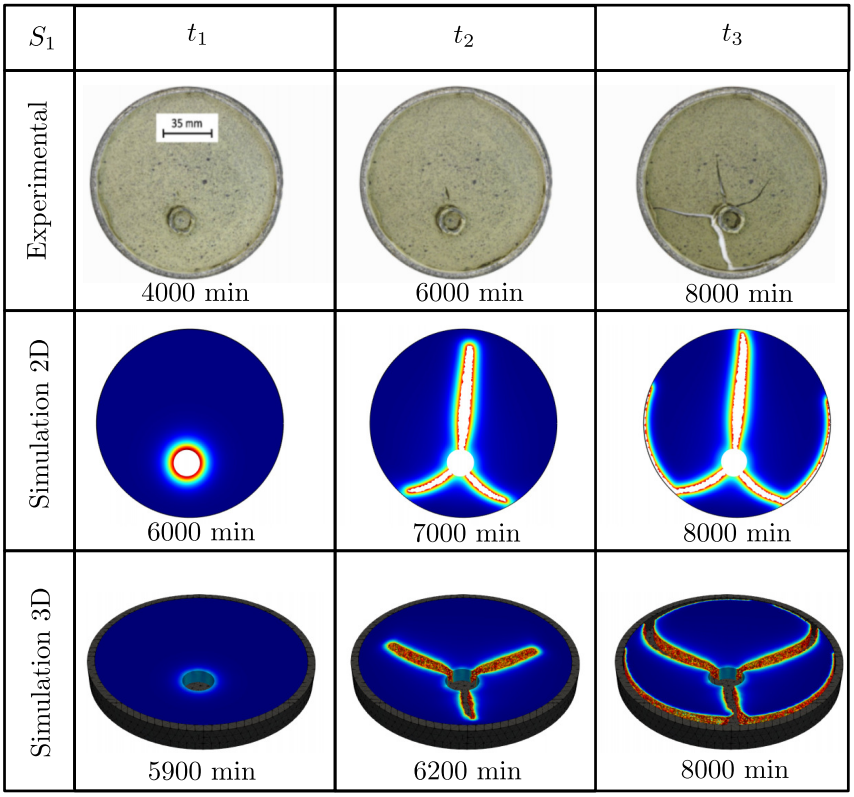

Figure 14: Crack pattern in S_1.

simulations, even when cracks are not initiated (see Fig. 20). The compression ring around the inclusion is reproduced well by the simulation model.

We note that the strain localizes in the vicinity of the cracks in both the experiments and simulations. The graphic representations were adapted by thresholding the damage to $d = 0.8$.

5.3. Deviatoric strains

In Figs. 21-24, local deviatoric strains measured experimentally as described in Section 2.1.3 are compared with the numerical simulation results.

The conclusions are similar to those for spherical strains. Even though the global distribution is satisfactorily reproduced by the numerical model at the beginning of the simulation (without cracks), regions of deviatoric strain local-

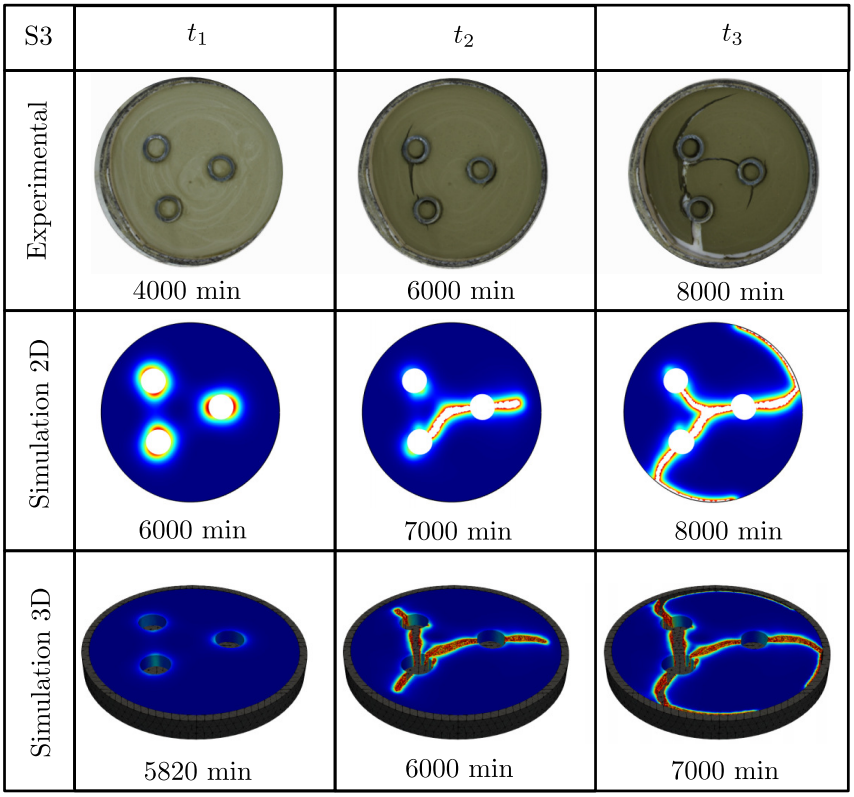

Figure 15: Crack pattern in S_3.

ization near the external boundary that are observed experimentally are not reproduced by the present model. The origin of this phenomenon has not yet been clearly identified. However, once the cracks propagate, the simulation generates a dilatation deformation of high intensity along its path, as in the experiment.

5.4. Remarks about experimental variability

As expected, the experiments show a major influence of the presence and positions of the inclusions on the final crack patterns. Another important observation is that in all of the experiments presented in this study, the cracks initiate from the boundary of the inclusions and then propagate into the matrix to the external boundary of the sample. This is also shown in the strain fields,

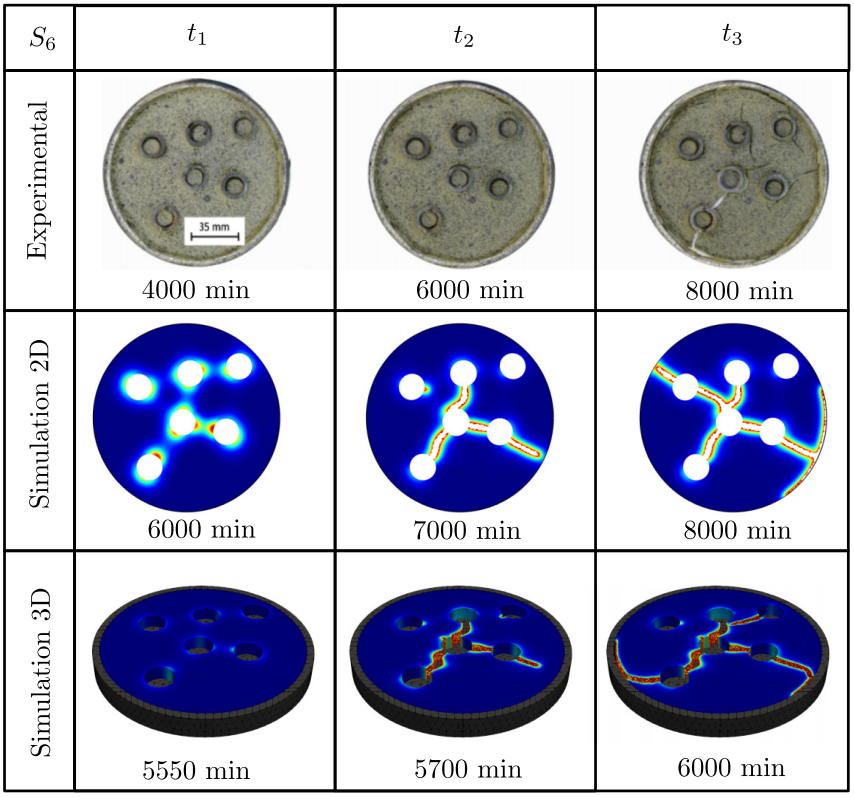

Figure 16: Crack pattern in S_6.

which exhibit strain concentrations near the boundaries of the inclusions at the early stages of the experiments, while this is not the case away from the inclusions. However, the deformation and cracking patterns are also characterized by a strong stochastic nature, as illustrated in Fig. 25. Here, three experimental realizations of the S_3 test were performed. It can be seen that the final crack geometry and local strain fields can differ significantly. We can assume that several phenomena are at the origin of the variability in the final crack distribution, listed as follows.

1. The friction on the bottom of the sample was experimentally limited by the application of a Teflon layer. However, this surface interaction remains to be quantified. Numerical studies on an experimental basis [46, 47] have

Exp.	2D simulation agreement	3D simulation agreement
S_{1c}		
3 cracks initiated from the inclusion and developing radially	Good agreement	Partial agreement: 2 cracks initiated from the inclusion but branching
S_1		
4 cracks initiated from the inclusion and developing radially	Partial agreement: 3 cracks initiated from the inclusion and developing radially	Partial agreement: 3 cracks initiated from the inclusion and developing radially
S_3		
Several cracks initiated from the inclusions	Good agreement	Good agreement
Inclusions cracks merge and propagate to the external boundary	Good agreement	Good agreement
S_5		
Several cracks initiated from the inclusions	Good agreement	Good agreement
Inclusions cracks merge and propagate to the external boundary	Good agreement	Good agreement

Table 3: Qualitative comparisons between experimental and simulated crack patterns during shrinkage of clay samples.

investigated the influence of this interaction on the cracking process.

2. The material parameters within the sample are time-dependent and heterogeneous at the micro-scale. The drying process may increase these heterogeneities. For example, the local fluctuations observed in the cen-

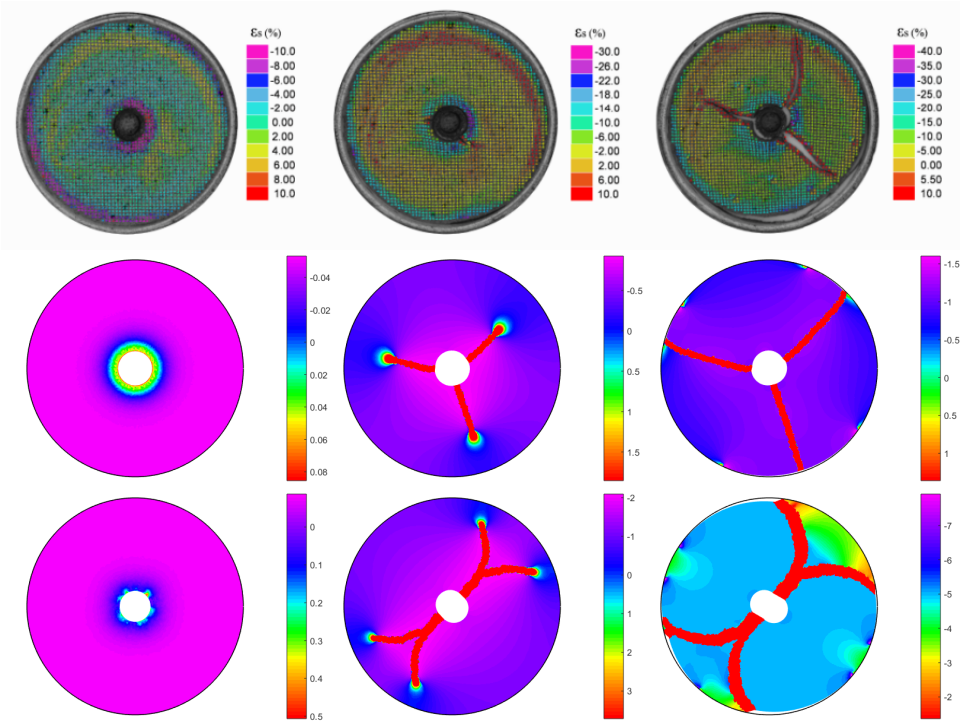

Figure 17: Spherical strain map in S_{1C}: experimental results (top), numerical results in 2D (middle), and numerical results in 3D (bottom); the times are the same than in Fig. 13.

tral part of the S_1 sample (see Fig. 18) may be associated with such constitutive heterogeneities.

3. The debonding at the external surface of the sample occurs randomly during the experiments.

To investigate the effects of decohesion on the boundary, we conducted additional simulations, as shown in Fig. 26, where debonding was artificially induced at several locations on the external boundary. From Fig. 26, we can note that the location of decohesion on the boundary has a strong impact on the distributions of cracks within the sample and seems to be consistent with the experimental observations in Fig. 25. It is worth noting that in all cases, the cracks still started from the inclusion boundaries and propagated to the external boundary, which was also observed experimentally.

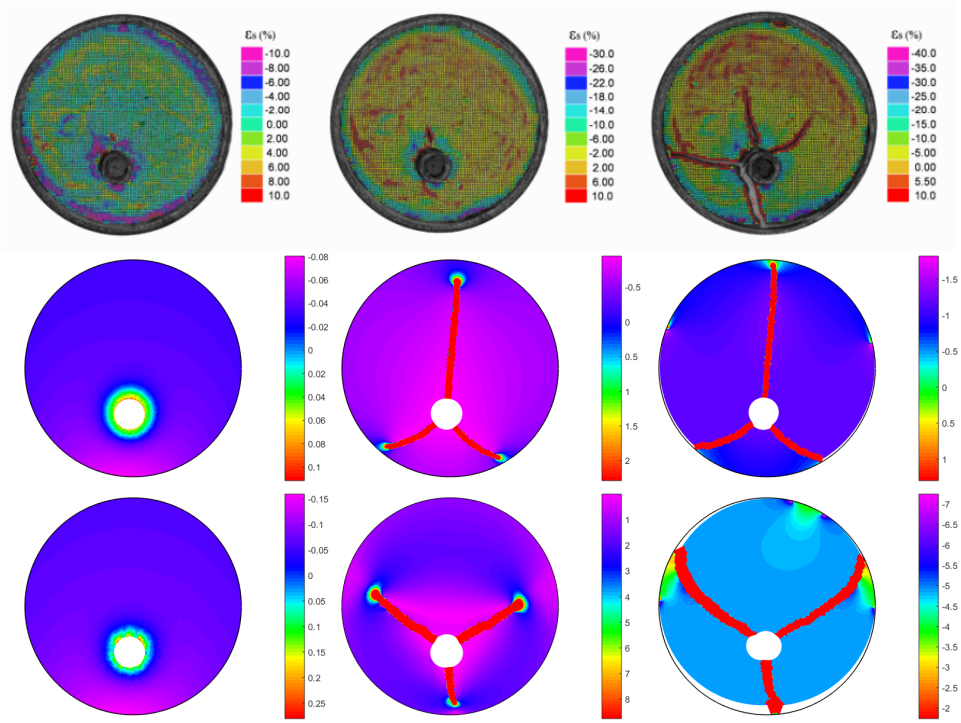

Figure 18: Spherical strain map in S_1: experimental results (top), numerical results in 2D (middle), and numerical results in 3D (bottom); the times are the same than in Fig. 14.

5.5. Discussion

In the above comparisons, we observed some partial, yet encouraging, qualitative agreement between the experiments and simulations. Globally, the initiation of cracks is well reproduced near the inclusions, and the propagation paths between inclusions and to the external boundary of the samples are well reproduced by the model. The global shrinkage of the sample is modeled satisfactorily through both spherical and deviatoric strains for simple configurations, but zones of localizations observed in the experiments are not captured by the present model. Possible reasons for the observed discrepancies and suggestions for future investigations are summarized as follows.

1. The zero-displacement boundary condition applied at the outer edge is a first approximation of the frictional forces that prevent the clay matrix

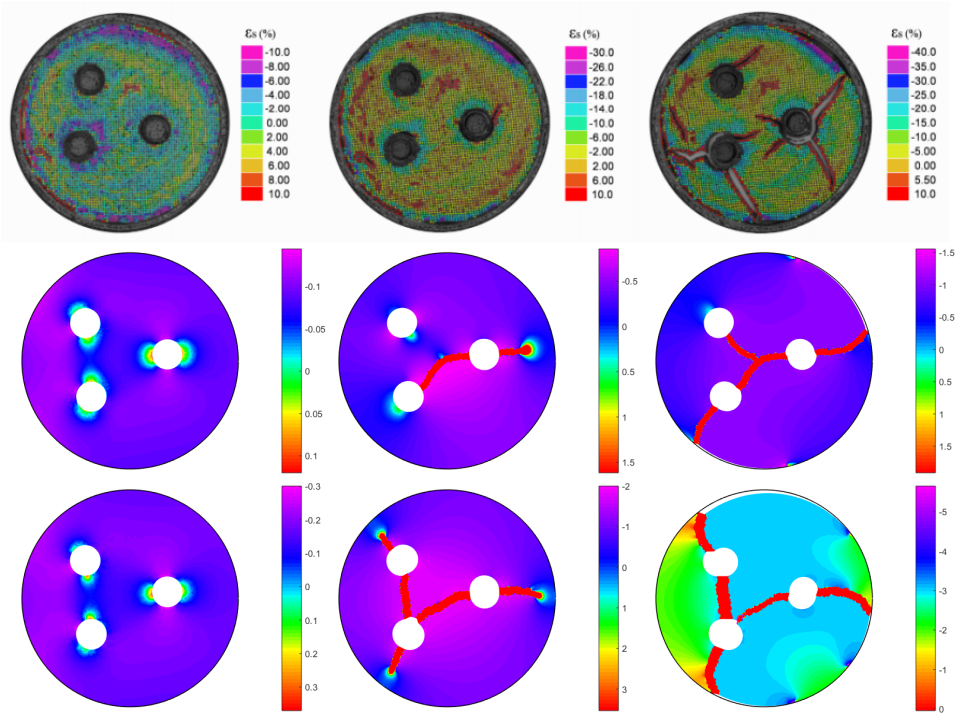

Figure 19: Spherical strain map S_3: experimental results (top), numerical results in 2D (middle), and numerical results in 3D (bottom); the times are the same than in Fig. 15.

from shrinking freely, hence creating the conditions for cracking. However, it was observed that the clay matrix slightly lifted off the bottom at the edges, and the amplitude of this phenomenon increased with time. To illustrate this point, results are shown in Fig. **??** where the sample is not restrained on its outer edges, but in a zone of small thickness close to the edges and in the clay. In this case, the edge effects observed experimentally are qualitatively reproduced.

2. A localized, compressive strain zone is experimentally observed close to the outer edge and at the interface between the inclusions and the matrix. This complex interface phenomenon requires further study and is presently not captured by our model.

3. The parameters that were used in the simulations were considered to be

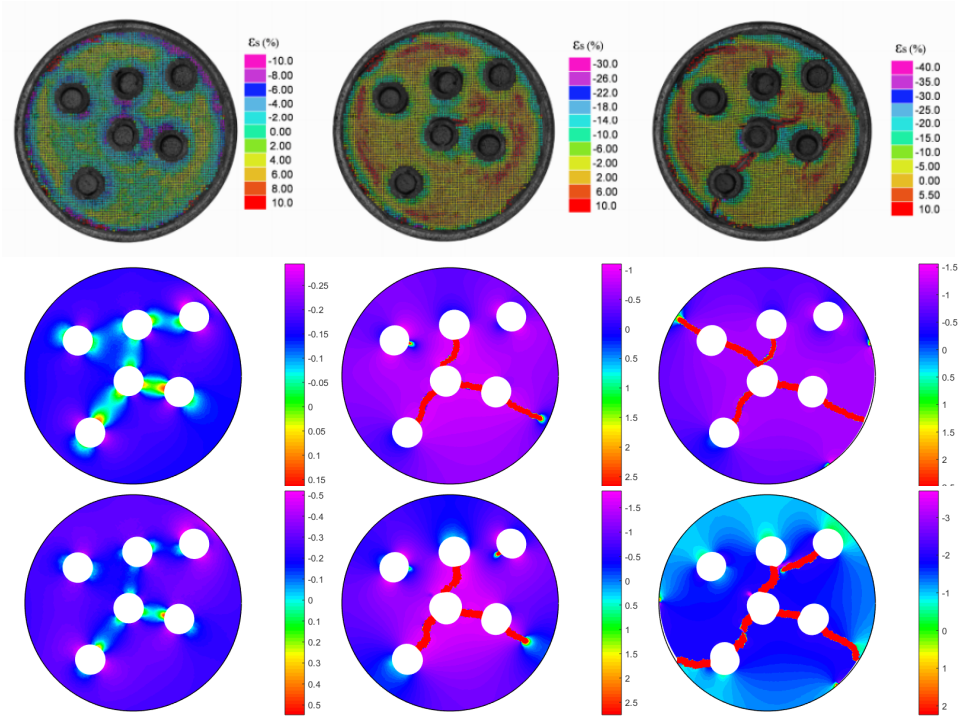

Figure 20: Spherical strain map in S_6: experimental results (top), numerical results in 2D (middle), and numerical results in 3D (bottom); the times are the same than in Fig. 16.

constants. However, some experimental results available in the literature suggest that these parameters may vary spatially and depend on the water content. In this context, a more advanced experimental campaign involving variable water contents could enhance the predictive capability of the computational model.

4. A large discrepancy is also observed in terms of the crack propagation velocity (quantified by the crack extension in a quasi-static regime). While crack propagation is typically observed over long time periods in the experiments (approximately 3000 to 4000 min), the crack propagation is approximately 10 to 20 times faster in the corresponding simulations.
5. The frictional forces on the bottom of the specimen are not included in the present model.

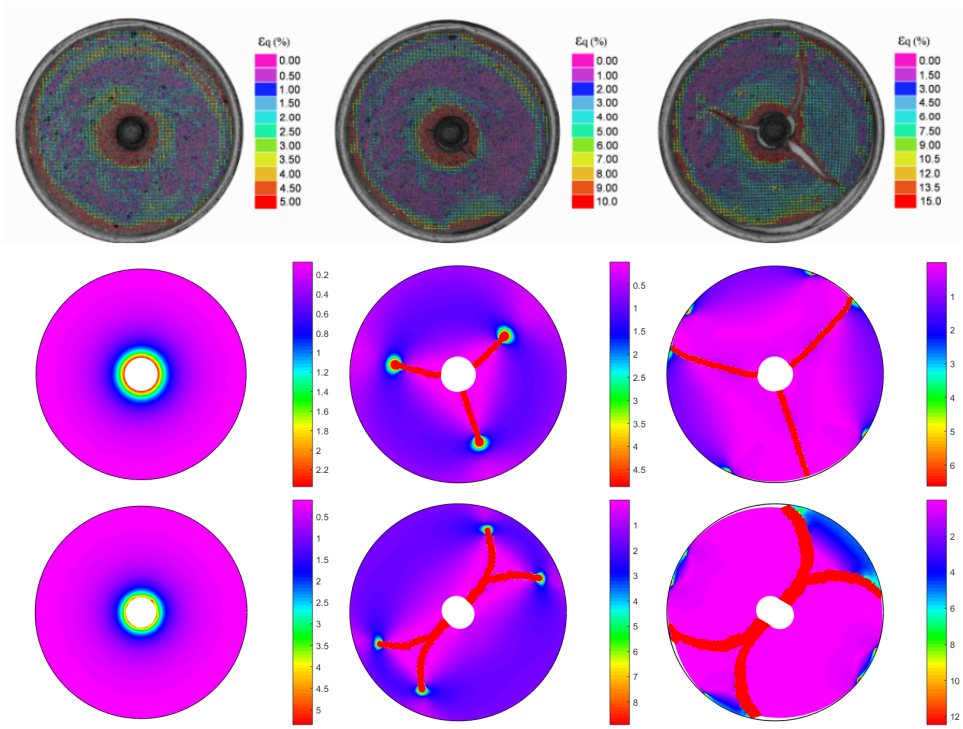

Figure 21: Deviatoric strain map in S_{1C}: experimental results (top), numerical results in 2D (middle), and numerical results in 3D (bottom); the times are the same than in Fig. 13.

6. As shown in Fig. 26, debonding of the sample at the external boundary has a direct impact on the local crack path. In our simulations, the cohesion at the external boundaries is assumed to be perfect until a crack reaches the external boundary.

545 7. The different sources of uncertainties mentioned in Section 5.4 are not included in the numerical model, which is another large source of discrepancies. Therefore, more quantitative comparisons should involve statistical data instead of direct deterministic comparisons.

6. Conclusion

550 In this study, we provided experimental results for a heterogeneous clay sample during desiccation and compared them with a numerical simulation model.

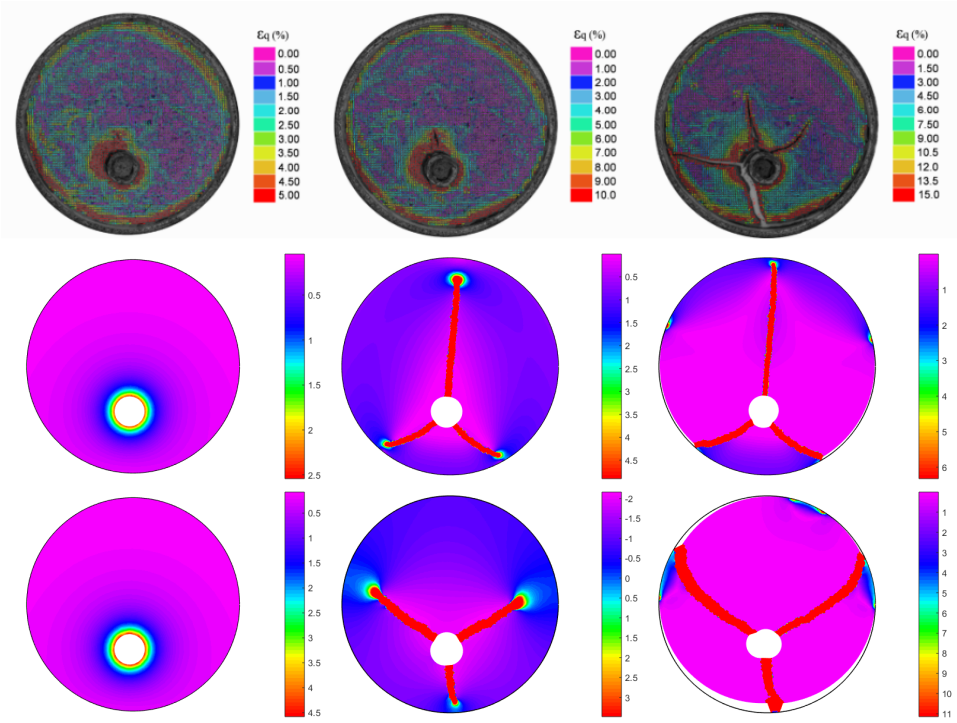

Figure 22: Deviatoric strain map in S_1: experimental results (top), numerical results in 2D (middle), and numerical results in 3D (bottom); the times are the same than in Fig. 14.

The main contributions and results of this study are highlighted as follows.

- We provided original experimental results for clay samples containing rigid inclusions, inducing more localized strain fields and a reduction in the uncertainties related to crack propagation during drying.
- For samples including one, three, and six inclusions, we provided experimental observations of final crack paths as well as local strain fields using DIC.
- We observed that in all cases, the cracks initiated from inclusion boundaries and then propagated to the external boundary of the sample.
- It was shown that debonding of the sample from the external boundary strongly affected the direction and number of cracks.

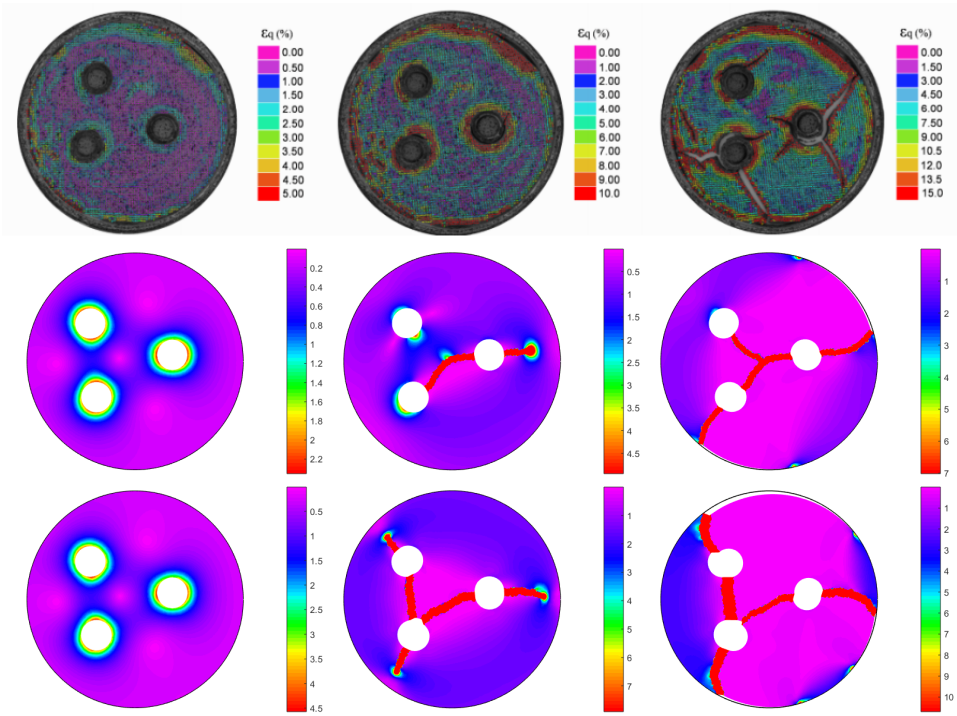

Figure 23: Deviatoric strain map in S_3: experimental results (top), numerical results in 2D (middle), and numerical results in 3D (bottom); the times are the same than in Fig. 15.

- A numerical continuous crack propagation model based on a phase field was used to simulate the heterogeneous shrinking process and for comparison with the experiments.

- While good qualitative agreement with the experimental results was generally observed, several discrepancies remain: (i) in the experiments, a region of compressive strain occurs near the external boundary, which is not reproduced in the simulations; (ii) the global compressive strain within the samples observed experimentally is well reproduced by the model, but local strains remain poorly captured; (iii) crack paths, including the number of cracks, directions, and branching is only qualitatively reproduced by the numerical model.

- We introduced a discussion of the possible sources of these discrepancies,

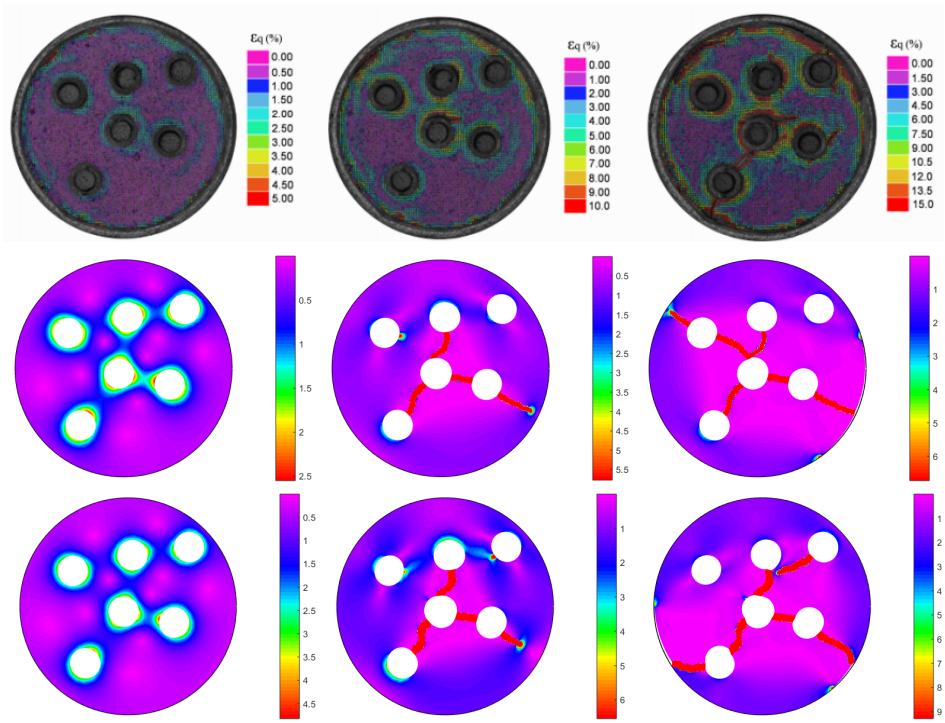

Figure 24: Deviatoric strain map in S_6: experimental results (top), numerical results in 2D (middle), and numerical results in 3D (bottom); the times are the same than in Fig. 16.

Figure 25: Different crack patterns observed for the same configuration with 3 inclusions.

including: (i) uncertainties related to external boundary decohesion and variations in local material parameters; (ii) the frictional effects of the lower boundary during drying; and (iii) the possibility of a more complex hydro-thermo-mechanical coupling, especially during the phase change of the clay matrix from liquid to solid, which is not included in the present

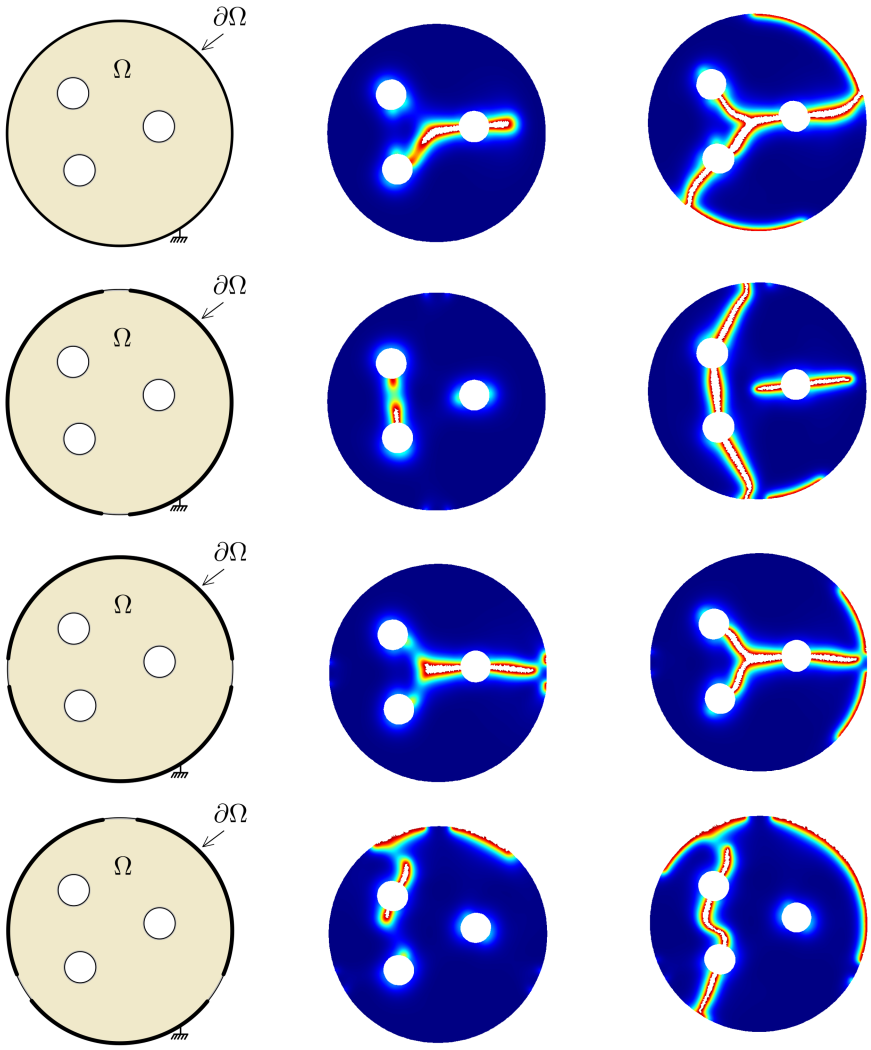

Figure 26: 2D crack evolution for different wall debonding locations: boundaries conditions, initiation and crack paths.

model.

7. Acknowledgements

The authors gratefully acknowledge the financial support from the LABEX Multi-Scale Modeling & Experimentation of Materials for Sustainable Construction (MMCD) through ANR Investments for the Future program ANR-11-LABX-022-01.

References

[1] X. Ma, J. Lowensohn, J. C. Burton, Universal scaling of polygonal desiccation crack patterns, Physical Review E 99 (1) (2019) 012802.

[2] W. Qi, Z.-y. Zhang, C. Wang, Y. Chen, Z.-m. Zhang, Crack closure and flow regimes in cracked clay loam subjected to different irrigation methods, Geoderma 358 (2020) 113978.

[3] R. A. Stirling, D. G. Toll, S. Glendinning, P. R. Helm, A. Yildiz, P. N. Hughes, J. D. Asquith, Weather-driven deterioration processes affecting the performance of embankment slopes, Géotechnique (2020) 1–13.

[4] Z. Yu, O. Eminue, R. Stirling, C. Davie, S. Glendinning, Desiccation cracking at field scale on a vegetated infrastructure embankment, Géotechnique Letters (2021) 1–21.

[5] J. Cordero, G. Useche, P. Prat, A. Ledesma, J. Santamarina, Soil desiccation cracks as a suction–contraction process, Géotechnique Letters 7 (4) (2017) 279–285.

[6] R. Tollenaar, L. Van Paassen, C. Jommi, Observations on the desiccation and cracking of clay layers, Engineering Geology 230 (2017) 23–31.

[7] S. Costa, J. Kodikara, S. Barbour, D. Fredlund, Theoretical analysis of desiccation crack spacing of a thin, long soil layer, Acta Geotechnica 13 (1) (2018) 39–49.

[8] T. Shepidchenko, J. Zhang, X. Tang, T. Liu, Z. Dong, G. Zheng, L. Yang, Experimental study of the main controlling factors of desiccation crack formation from mud to shale, Journal of Petroleum Science and Engineering (2020) 107414.

[9] H. Zeng, C.-S. Tang, Q. Cheng, C. Zhu, L.-Y. Yin, B. Shi, Drought-induced soil desiccation cracking behavior with consideration of basal friction and layer thickness, Water Resources Research 56 (7) (2020) e2019WR026948.

[10] K. M. Crosby, R. M. Bradley, Fragmentation of thin films bonded to solid substrates: Simulations and a mean-field theory, Physical Review E 55 (5) (1997) 6084.

[11] K.-t. Leung, Z. Néda, Pattern formation and selection in quasistatic fracture, Physical review letters 85 (3) (2000) 662.

[12] S. Sadhukhan, T. Dutta, S. Tarafdar, Crack formation in composites through a spring model, Physica A: Statistical Mechanics and its Applications 390 (4) (2011) 731–740.

[13] A. Malthe-Sørenssen, T. Walmann, J. Feder, T. Jøssang, P. Meakin, H. Hardy, Simulation of extensional clay fractures, Physical Review E 58 (5) (1998) 5548.

[14] A. Ghavam-Nasiri, A. El-Zein, D. Airey, R. K. Rowe, A. Bouazza, Numerical simulation of geosynthetic clay liner desiccation under high thermal gradients and low overburden stress, International Journal of Geomechanics 19 (7) (2019) 04019069.

[15] J. Sima, M. Jiang, C. Zhou, Numerical simulation of desiccation cracking in a thin clay layer using 3d discrete element modeling, Computers and Geotechnics 56 (2014) 168–180.

[16] M. S. El Youssoufi, J.-Y. Delenne, F. Radjai, Self-stresses and crack formation by particle swelling in cohesive granular media, Physical Review E 71 (5) (2005) 051307.

[17] H. Péron, J. Delenne, L. Laloui, M. El Youssoufi, Discrete element modelling of drying shrinkage and cracking of soils, Computers and Geotechnics 36 (1-2) (2009) 61–69.

[18] J. Zhang, Y. Lu, L. He, L. Yang, Y. Ni, Modeling progressive interfacial debonding of a mud-crack film on elastic substrates, Engineering Fracture Mechanics 177 (2017) 123–132.

[19] Y. Gui, Z. Zhao, J. Kodikara, H. H. Bui, S.-Q. Yang, Numerical modelling of laboratory soil desiccation cracking using udec with a mix-mode cohesive fracture model, Engineering Geology 202 (2016) 14–23.

[20] T. D. Vo, A. Pouya, S. Hemmati, A. M. Tang, Numerical modelling of desiccation cracking of clayey soil using a cohesive fracture method, Computers and Geotechnics 85 (2017) 15–27.

[21] M. Sánchez, O. L. Manzoli, L. J. Guimarães, Modeling 3-d desiccation soil crack networks using a mesh fragmentation technique, Computers and Geotechnics 62 (2014) 27–39.

[22] J. Liang, R. Huang, J. Prevost, Z. Suo, Evolving crack patterns in thin films with the extended finite element method, International Journal of Solids and Structures 40 (10) (2003) 2343–2354.

[23] T. Hu, J. Guilleminot, J. E. Dolbow, A phase-field model of fracture with frictionless contact and random fracture properties: Application to thin-film fracture and soil desiccation, Computer Methods in Applied Mechanics and Engineering 368 (2020) 113106.

[24] G. A. Francfort, J.-J. Marigo, Revisiting brittle fracture as an energy minimization problem, Journal of the Mechanics and Physics of Solids 46 (8) (1998) 1319–1342.

[25] B. Bourdin, G. A. Francfort, J.-J. Marigo, The variational approach to fracture, Journal of elasticity 91 (1-3) (2008) 5–148.

[26] C. Miehe, M. Hofacker, F. Welschinger, A phase field model for rate-independent crack propagation: Robust algorithmic implementation based on operator splits, Computer Methods in Applied Mechanics and Engineering 199 (2010) 2765–2778. doi:10.1016/j.cma.2010.04.011.

[27] L.-L. Wang, C.-S. Tang, B. Shi, Y.-J. Cui, G.-Q. Zhang, I. Hilary, Nucleation and propagation mechanisms of soil desiccation cracks, Engineering Geology 238 (2018) 27–35.

[28] M. Audiguier, Z. Geremew, S. Laribi, R. Cojean, Caractérisation au laboratoire de la sensibilité au retrait-gonflement des sols argileux, Revue française de Géotechnique (120-121) (2007) 67–82.

[29] G. Zemenu, A. Martine, C. Roger, Analysis of the behaviour of a natural expansive soil under cyclic drying and wetting, Bulletin of engineering geology and the environment 68 (2009) 421–436.

[30] C.-S. Tang, B. Shi, C. Liu, W.-B. Suo, L. Gao, Experimental characterization of shrinkage and desiccation cracking in thin clay layer, Applied Clay Science 52 (1-2) (2011) 69–77.

[31] C.-S. Tang, B. Shi, Y.-J. Cui, C. Liu, K. Gu, Desiccation cracking behavior of polypropylene fiber–reinforced clayey soil, Canadian Geotechnical Journal 49 (9) (2012) 1088–1101.

[32] M. Bornert, J. Orteu, S. Roux, Mesures de champs et identification en mécanique des solides, chapter corrélation d'images, Hermes, Lavoisier (2011).

[33] L. Allais, M. Bornert, T. Bretheau, D. Caldemaison, Experimental characterization of the local strain field in a heterogeneous elastoplastic material, Acta Metallurgica et materialia 42 (11) (1994) 3865–3880.

[34] M. Borden, T. J. Hughes, C. M. Landis, C. V. Verhoosel, A higher-order phase-field model for brittle fracture: Formulation and analysis within the

isogeometric analysis framework, Computer Methods in Applied Mechanics and Engineering 273 (2014) 100–118.

[35] M. Ambati, T. Gerasimov, L. de Lorenzis, A review on phase-field models of brittle fracture and a new fast hybrid formulation, Computational Mechanics 55 (2) (2015) 383–405.

[36] T. Nguyen, J. Yvonnet, Q.-Z. Zhu, M. Bornert, C. Chateau, A phase-field method for computational modeling of interfacial damage interacting with crack propagation in realistic microstructures obtained by microtomography, Computer Methods in Applied Mechanics and Engineering (312) (2016) 567–595.

[37] P. Areias, T. Rabczuk, M. Msekh, Phase-field analysis of finite-strain plates and shells including element subdivision, Computer Methods in Applied Mechanics and Engineering 312 (2016) 322–350.

[38] G. El Mountassir, M. Sánchez, E. Romero, An experimental study on the compaction and collapsible behaviour of a flood defence embankment fill, Engineering geology 179 (2014) 132–145.

[39] T. Cajuhi, L. Sanavia, L. De Lorenzis, Phase-field modeling of fracture in variably saturated porous media, Computational Mechanics 61 (3) (2018) 299–318.

[40] M. R. Lakshmikantha, Experimental and theoretical analysis of cracking in drying soils, Ph.D. thesis, Universitat Politècnica de Catalunya (2009).

[41] H. Peron, L. Laloui, T. Hueckel, L. B. Hu, Desiccation cracking of soils, European journal of environmental and civil engineering 13 (7-8) (2009) 869–888.

[42] T. T. Nguyen, J. Yvonnet, M. Bornert, C. Chateau, K. Sab, R. Romani, R. Le Roy, On the choice of parameters in the phase field method for simulating crack initiation with experimental validation, International Journal of Fracture 197 (2) (2016) 213–226.

[43] J. Kodikara, S. Costa, Desiccation cracking in clayey soils: mechanisms and modelling, in: Multiphysical testing of soils and shales, Springer, 2013, pp. 21–32.

[44] J.-J. Wang, J.-G. Zhu, C. Chiu, H. Zhang, Experimental study on fracture toughness and tensile strength of a clay, Engineering Geology 94 (1-2) (2007) 65–75.

[45] M. Lakshmikantha, P. Prat, A. Ledesma, Image analysis for the quantification of a developing crack network on a drying soil, Geotechnical Testing Journal 32 (6) (2009) 505–515.

[46] J. Sima, M. Jiang, C. Zhou, Numerical simulation of desiccation cracking in a thin clay layer using 3d discrete element modeling, Computers and Geotechnics 56 (2014) 168–180.

[47] A. L. Amarasiri, J. K. Kodikara, S. Costa, Numerical modelling of desiccation cracking, International Journal for Numerical and Analytical Methods in Geomechanics 35 (1) (2011) 82–96.